IEEE Access
Multidisciplinary | Rapid Review | Open Access Journal

Received 28 May 2022, accepted 20 June 2022, date of publication 27 June 2022, date of current version 30 June 2022.

Digital Object Identifier 10.1109/ACCESS.2022.3186302

RESEARCH ARTICLE

Ultrasound Imaging of Bottom Opening Crack Based on Frequency-Domain Reverse Time Migration

CONGCONG WANG[1], KUN WANG[2], JING ZHU[3], DEXIU DONG[4], AND JUNJIE CHANG[1]

[1]Key Laboratory of Nondestructive Testing, Ministry of Education, Nanchang Hangkong University, Nanchang 330063, China
[2]Tokyo Institute of Technology, Tokyo 152-8550, Japan
[3]Research Center for Humanoid Sensing, Zhejiang Lab, Hangzhou 311121, China
[4]AECC Shenyang Liming Aero-Engine Company Ltd., Shenyang 110043, China

Corresponding author: Kun Wang (3482832327@qq.com)

This work was supported by the National Natural Science Foundation of China under Grant 11464030.

ABSTRACT In 2-dimension (2D), a frequency-domain reverse time migration (FRTM) based on the optimal 9-point finite difference method (FDM) is introduced into the field of ultrasonic non-destructive testing (NDT). This study solves the challenge that conventional ultrasound imaging methods are difficult to image defects completely. In numerical investigations, the use of multiple reflection waves and the necessity of bottom identification are explained. In actual inspection, the method of bottom identification is given, and then the bottom opening crack (BOC) of different lengths in the aluminum block can be completely imaged. Furthermore, the conventional total focusing method (TFM) cannot image the sides of the BOCs using the same data as FRTM. Therefore, the quantitative analysis of BOC based on the complete imaging results of FRTM is more convincing. On this basis, the optimization methods for the number of grid points placed at each wavelength and the frequency calculation range are also given. On the premise of ensuring high image quality, the imaging computation time is reduced to 1/18 of the original, which improves the computing efficiency of the FRTM.

INDEX TERMS Frequency-domain, reverse time migration, bottom identification, quantitative analysis, image quality evaluation.

I. INTRODUCTION

In engineering structures, fatigue cracks can occur in metal materials under long-term cyclic loading, which will increase the possibility of metal materials failure [1], [2]. Generally, ultrasonic array imaging technology can image fatigue defects in the workpiece, making inspection results more intuitive [3]–[6]. However, the traditional ultrasonic array imaging method can only obtain the image of the upper surface or the upper end of the defect. Since most of the echo information on the side and bottom of the defect is reflected multiple times, the multiple reflected waves cannot be fully used by the conventional ultrasound array imaging method. Although half-ship TFM [7] can use multiple reflected waves, in order not to overwhelm the energy of multiple reflected waves with the main power, the transducer should not be placed above the defect but on the side of the defect. Therefore, this method can only image one side of the BOC. The transducer can be placed above the defect in the reverse time migration (RTM) method. The multiple reflection waves from the defect can be fully utilized based on the two-way wave equation so that the defect can be completely imaged. It can be regarded as a matched filter between the incident acoustic field and the time-reversed received acoustic field [8]. RTM has been considered one of the most precise imaging methods [9]. Therefore, this paper chooses RTM for research and applies it to ultrasonic NDT.

In this study, an FRTM based on the optimal 9-point FDM is introduced into the field of ultrasonic NDT. The method enables complete imaging of the defect and requires only

The associate editor coordinating the review of this manuscript and approving it for publication was Riccardo Carotenuto.

partial frequency components and 4 grid points per wavelength. Compared with other RTM methods, such as the time-domain and Fourier method [10], [11], this method can significantly reduce unnecessary calculations because the frequency band of the ultrasonic signal is generally larger, and many unnecessary high-frequency and low-frequency components can be skipped during calculation.

Inspired by the RTM method, time-domain reverse time migration (TRTM) has been proposed for use in ultrasonic NDT. Müller et al. imaged vertical interfaces and circular voids in concrete using the TRTM based on FDM [12]. Beniwal *et al.* located the rebar and distinguished the layering and bonding state of the rebar using the RTM based on FDM [13]. Similarly, Qi *et al.* inspected the grouting quality of the connecting casing in the prefabricated building using the TRTM based on FDM and imaged the case of the semi-grouted state [14]. These early studies indicate the great potential of the RTM in ultrasonic NDT.

On the other hand, Rao *et al.* imaged a branched surface-breaking notch and an embedded stepped notch using the TRTM based on FDM [15]. But this TRTM method needs about 15-20 grids per wavelength to meet the acoustic field's spatial and temporal sampling conditions, which incurs many computational costs. Lubeigt et al. imaged holes and oblique slits, but the method used is a time-domain topological imaging method that cannot be imaged using only partial frequency components when dealing with frequency-dependent media [16]. Chang et al. discussed the absorption boundary and imaging conditions in the TRTM based on FDM and performed complete imaging of a curved and bifurcated BOC [17], but the computational efficiency of imaging was not optimized. Yang et al. imaged multiple side-drilled holes in an aluminum block using a multistep angular spectrum approach [18]. But this is a Fourier method, and it is hard to skip unnecessary high-frequency and low-frequency calculations. The FRTM algorithm proposed by Liu et al. submitted imaging results almost identical to the conventional TRTM algorithm, reducing the computation time by two orders of magnitude. Moreover, it can provide critical information for China's Chang-E 5 lunar exploration mission [19].

Therefore, an FRTM based on the optimal 9-point FDM is introduced into the field of ultrasonic NDT. This study fully describes this imaging method, including the imaging and optimization methods.

Furthermore, this paper is organized as follows. The principle of the FRTM is introduced in Section 2. In Section 3, the BOC simulation model in the aluminium blocks is set in MATLAB. In the simulation, it is confirmed that the bottom identification is a necessity for complete imaging. In Section 4, the experimental system is set up. Based on the experimental data, a method of bottom identification is proposed so that defects can be fully imaged and FRTM is compared with TFM. A very intuitive quantitative analysis of the defect is possible based on the complete imaging results. Finally, the computational efficiency of this algorithm is optimized. In Section 5, other details of this paper are discussed. The conclusions and descriptions of future work are shown in Section 6.

II. METHODS

The three main steps of FRTM are consistent with TRTM and mainly include [20]: (1) The forward propagation of the acoustic source field; (2) The back propagation of the receiving acoustic field; (3) Reconstructing the image under imaging conditions.

A. WAVE FIELD EXTRAPOLATION SCHEME

The scalar wave equation for a homogeneous isotropic medium is calculated in the frequency-domain as follows:

$$\nabla^2 P + \frac{\omega^2}{v^2} P = 0, \tag{1}$$

where ∇ denotes the Nabla operator, P and v are the acoustic pressure field and the acoustic velocity of the medium, respectively; ω is the angular frequency, as we all know, $\omega = 2\pi f$, and f is the frequency.

In 2D, the optimal 9-point FDM can be used for acoustic field extrapolation [21]. An example of the setting point (m, n) and its nearest 8 points in the FDM are shown in Fig. 1.

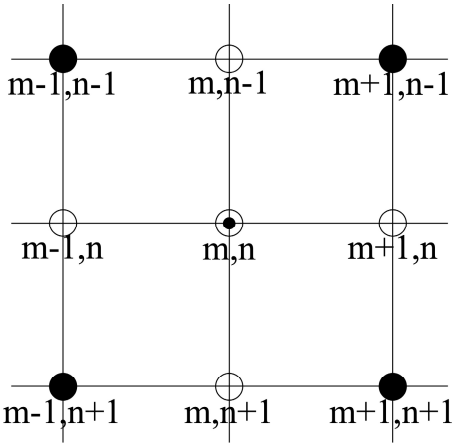

FIGURE 1. The setting point (m, n) and its nearest 8 points in the FDM.

Using the optimal 9-point operator to approximate the Laplace term and the mass acceleration term, the Eq. (1) can be formulated as

$$\begin{aligned} &a\frac{\left(P_{\mathrm{m+1,n}}+P_{\mathrm{m-1,n}}-4P_{\mathrm{m,n}}+P_{\mathrm{m,n+1}}+P_{\mathrm{m,n-1}}\right)}{\Delta^2}+(1-a)\\ &\frac{\left(P_{\mathrm{m+1,n+1}}+P_{\mathrm{m-1,n+1}}-4P_{\mathrm{m,n}}+P_{\mathrm{m+1,n-1}}+P_{\mathrm{m-1,n-1}}\right)}{\Delta^2}\\ &+\frac{\omega^2}{v^2}\left[cP_{\mathrm{m,n}}+d\left(P_{\mathrm{m+1,n}}+P_{\mathrm{m-1,n}}+P_{\mathrm{m,n+1}}\right.\right.\\ &\left.+P_{\mathrm{m,n-1}}\right)+\frac{(1-c-4d)}{4}\left(P_{\mathrm{m+1,n+1}}+P_{\mathrm{m-1,n+1}}\right.\\ &\left.\left.+P_{\mathrm{m+1,n-1}}+P_{\mathrm{m-1,n-1}}\right)\right]=0, \end{aligned} \tag{2}$$

where $a = 0.5461$, $c = 0.6248$, and $d = 0.09381$ are defined. The coefficients are solved by minimizing the numerical solution error of the phase velocity [21].

According to the complete stencil involving nine points described by Eq. (22) in Ref. [22], the coefficients corresponding to the 9 points in Fig.1 and Eq. (2) can be obtained. It can be seen from Ref. [22] that the coefficients are related to the bulk modulus and the density. These 9 points can be extended to the entire sound field, and a large coefficient matrix is obtained, which is the complex impedance matrix. This complex impedance matrix is converted to a sparse matrix to save computer memory, and a sparse matrix $\boldsymbol{M}$ can be obtained. When solving large systems of equations, LU decomposition can significantly reduce the computational cost, and $\boldsymbol{M}$ is performed LU decomposition, as shown in Eq. 3.

$$[\boldsymbol{L}, \boldsymbol{U}, \boldsymbol{P}, \boldsymbol{O}] = \mathrm{LU}(\boldsymbol{M}), \tag{3}$$

where $\boldsymbol{L}$ is a unit lower triangular matrix, $\boldsymbol{U}$ is an upper triangular matrix, $\boldsymbol{P}$ is a row permutation matrix, and $\boldsymbol{O}$ is a column permutation matrix.

Therefore, the frequency domain acoustic field $\boldsymbol{G}$ can be obtained in Eq. 4.

$$\boldsymbol{G} = \boldsymbol{O}\left[\frac{\boldsymbol{U}}{\left(\frac{\boldsymbol{L}}{\boldsymbol{PC}}\right)}\right], \tag{4}$$

where $\boldsymbol{C}$ is the acoustic source field.

This high-efficiency solution method has been described in detail in Ref. [22], and the optimization in this paper is based on this to improve the computational efficiency further.

When the acoustic source $\boldsymbol{C}$ is set as the excitation source, the forward extrapolated acoustic field of the acoustic source field can be obtained. Similarly, placing the acoustic source $\boldsymbol{C}$ as the received signal can get the reverse extrapolated acoustic field.

B. PERFECTLY MATCHED LAYER

Limited by memory capacity and calculating time, only a limited target area can be artificially intercepted for calculation. The second-order finite-difference wave equation with the perfectly matched layer (PML) absorbing boundary condition is given to eliminate boundary reflections as follows:

$$\begin{aligned}\frac{-\omega^2}{K_{\mathrm{m,n}}}P_{\mathrm{m,n}} = {} & \frac{1}{\xi_{\mathrm{r}}}\frac{1}{\Delta^2}\left[\frac{b_{\mathrm{m}+\frac{1}{2},\mathrm{n}}}{\xi_{\mathrm{r}+\frac{1}{2}}}\left(P_{\mathrm{m}+1,\mathrm{n}} - P_{\mathrm{m,n}}\right)\right. \\ & \left. - \frac{b_{\mathrm{m}-\frac{1}{2},\mathrm{n}}}{\xi_{\mathrm{r}-\frac{1}{2}}}\left(P_{\mathrm{m,n}} - P_{\mathrm{m}-1,\mathrm{n}}\right)\right] \\ & + \frac{1}{\xi_{\mathrm{s}}}\frac{1}{\Delta^2}\left[\frac{b_{\mathrm{m,n}+\frac{1}{2}}}{\xi_{\mathrm{s}+\frac{1}{2}}}\left(P_{\mathrm{m,n}+1} - P_{\mathrm{m,n}}\right)\right. \\ & \left. - \frac{b_{\mathrm{m,n}-\frac{1}{2}}}{\xi_{\mathrm{s}-\frac{1}{2}}}\left(P_{\mathrm{m,n}} - P_{\mathrm{m,n}-1}\right)\right] + C_{\mathrm{m,n}}, \end{aligned} \tag{5}$$

where, $K_{\mathrm{m,n}}$ is the bulk modulus at point (m, n); r and s are the local coordinates in the PML layer whose origins are located at the outer edges of the model; the inverse of the density is denoted by the buoyancy b, and the averaged coefficient $b_{\mathrm{m}+\frac{1}{2},\mathrm{n}} = \frac{1}{2}\left(b_{\mathrm{m}+1,\mathrm{n}} + b_{\mathrm{m,n}}\right)$; the averaged coefficient $\xi_{\mathrm{r}+\frac{1}{2}} = \frac{1}{2}\left(\xi_{\mathrm{r}+1} + \xi_{\mathrm{r}}\right)$, $\xi_{\mathrm{r}} = 1 + \frac{m\gamma_{\mathrm{r}}}{\omega}$, $\gamma_{\mathrm{r}} = c_{\mathrm{PML}}\cos\left(\frac{\pi}{2}\frac{r}{L}\right)$, L is the width of PML, and the scalar c_{PML} is defined by trial and error according to the width of the PML; Same as above, $\xi_{\mathrm{r}-\frac{1}{2}}$, ξ_{s}, $\xi_{\mathrm{s}+\frac{1}{2}}$, and $\xi_{\mathrm{s}-\frac{1}{2}}$ can also be derived; $C_{\mathrm{m,n}}$ is the acoustic source.

When performing extrapolation of the acoustic field, the absorption effect can be achieved by using equation (7) at the required boundaries. Here, the impact of PML is shown. After the acoustic field extrapolation in the frequency-domain, an inverse Fourier transform can be performed on the entire acoustic field, which converts the frequency-domain acoustic field to a time-domain acoustic field. And extract a snapshot of the acoustic field at a specific time, as shown in Fig. 2.

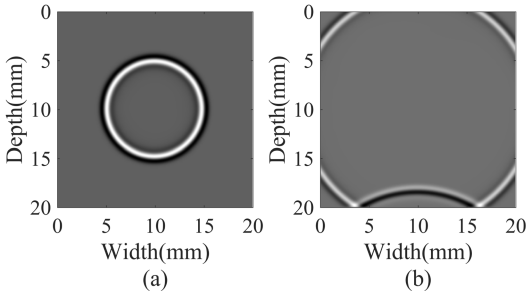

FIGURE 2. The acoustic field extrapolation and the absorption effect of PML. (a) The acoustic field at $1\ \mu s$; (b) The acoustic field at $2.1\ \mu s$.

In Fig. 2, a point source is set at the center of the 2D model, the Rake wavelet delayed by half a wavelength is applied as the excitation source, and the acoustic field is extrapolated. In this model, except for the bottom, 20 layers of PML are set at the other three boundaries; other parameters are consistent with the following Section 3. As shown in Fig. 2(b), it can be clearly seen those the reflected wave is produced only at the bottom, and the other three boundaries hardly see the reflected wave.

C. IMAGING CONDITIONS OF FRTM

The migration can generally be expressed as a zero-lag cross-correlation between the forward extrapolated acoustic field and the reverse extrapolated acoustic field [23], [24], and imaging result I is defined as

$$I = \frac{\int \mathrm{Real}\left(\boldsymbol{SR}\right) d\omega}{\int \mathrm{conj}\left(\boldsymbol{R}\right)\boldsymbol{R} d\omega}, \tag{6}$$

where Real means obtaining the real part of the complex number, conj means the conjugate transformation, $\boldsymbol{S}$ is the forward modeling acoustic field, $\boldsymbol{R}$ is the reverse extrapolated acoustic field.

Ref. [17] has demonstrated that this cross-correlation imaging condition produces better imaging results because it can use the received acoustic field to illuminate the imaging results. In addition, the imaging results are normalized by default in this study.

In the scheme, further enhancing the migration image and removing artifacts in the image, a 2D Laplacian filter is applied to the resulting migration image [25], [26]. The specific method is to use a kernel to convolve the image, and the kernel H of the 2D Laplacian is

$$H = \frac{4}{h+1}\begin{bmatrix} \frac{h}{4} & \frac{1-h}{4} & \frac{h}{4} \\ \frac{1-h}{4} & -1 & \frac{1-h}{4} \\ \frac{h}{4} & \frac{1-h}{4} & \frac{h}{4} \end{bmatrix}, \tag{7}$$

where h defaults to 0.

D. IMAGE QUALITY EVALUATION

It is necessary to adjust based on image quality evaluation (IQE) results to promote the optimization of grid points and frequency components in the FRTM. There are four main types of standard methods for IQE: Higher other metric (HOM), Entropy metric (EM), Contrast metric (CM), and Intensity metric (IM) [27], [28]. In 2D, the four evaluation formulas for the image matrix $I(x, z)$ are as follows.

(1) HOM

$$\mathrm{HOM\ (k)} = \frac{\sum_{m=1}^{M}\sum_{n=1}^{N}\left(|I(x_\mathrm{m}, z_\mathrm{n})| - \hat{\mu}\right)^k}{(MN-1)\hat{\sigma^k}}, \tag{8}$$

where $k \geq 1$, $\hat{\mu}$, $\hat{\sigma}$, M, and N are the mean, the standard deviation, the number of rows, and the number of columns of the image matrix I (x, z), respectively.

(2) EM

$$\mathrm{EM} = -\sum_{m=1}^{M}\sum_{n=1}^{N}\alpha(x_\mathrm{m}, z_\mathrm{n})\ln\left[\alpha(x_\mathrm{m}, z_\mathrm{n})\right], \tag{9}$$

where $\alpha(x_\mathrm{m}, z_\mathrm{n}) = \frac{|I(x_\mathrm{m}, z_\mathrm{n})|^2}{\sum_{m=1}^{M}\sum_{n=1}^{N}|I(x_\mathrm{m}, z_\mathrm{n})|}$.

(3) CM

$$\mathrm{CM\ (k)} = \frac{\sqrt{\sum_{m=1}^{M}\sum_{n=1}^{N}\left\{|I(x_\mathrm{m}, z_\mathrm{n})|^k - \alpha(x_\mathrm{m}, z_\mathrm{n})\right\}^2}}{\sum_{m=1}^{M}\sum_{n=1}^{N}|I(x_\mathrm{m}, z_\mathrm{n})|^k}, \tag{10}$$

where $\alpha(x_\mathrm{m}, z_\mathrm{n}) = \left(\frac{1}{MN}\right)\sum_{m=1}^{M}\sum_{n=1}^{N}|I(x_\mathrm{m}, z_\mathrm{n})|^k$ and $k = 1,\ 2$.

(4) IM

$$\mathrm{IM\ (k)} = \frac{\sum_{m=1}^{M}\sum_{n=1}^{N}|I(x_\mathrm{m}, z_\mathrm{n})|^k}{\left(\sum_{m=1}^{M}\sum_{n=1}^{N}|I(x_\mathrm{m}, z_\mathrm{n})|\right)^k}, \tag{11}$$

where $k = 2,\ 4$.

E. IMAGING STEPS OF FRTM

Step 1: The full matrix capture (FMC) data can be obtained by using ultrasonic arrays to collect data on the workpiece [3]. Generally, in the transmission and reception of the ultrasonic array, each element transmits ultrasonic waves in turn, then all the elements receive ultrasonic at the same time.

Step 2: A model consistent with the workpiece is built in a 2D Cartesian coordinate system using MATLAB [29]. The PML absorption boundaries are added as needed. Since the detected defect is unknown, the defect cannot be drawn in the model. This step prepares for subsequent acoustic field forward and reverse. In this step, a method for optimizing the procedure can exist. The number of grid points in the 2D Cartesian coordinate system can be reduced, and IQE is used to evaluate the final imaging results after the reduction of grid points.

Step 3: In 2D Cartesian coordinate system, one of the elements is used as the excitation source, and the acoustic field extrapolation is performed in the 2D frequency-domain using the method in Section 2.1, and the acoustic field information of each point in the 2D modeled area is saved.

Step 4: The time-domain discrete data collected by a single excitation in practice is converted into a frequency-domain signal using the fast Fourier transform (FFT), then the frequency-domain signal is applied to the original receiving position for reverse extrapolation of the acoustic field in a 2D Cartesian coordinate system. These are like step 2, and the acoustic field information of each point in the 2D modeled area is also saved. In this step, methods of optimizing the program can exist. The obtained frequency domain signal can be partially entered into the program to reduce the computational effort and use IQE to evaluate the final imaging results.

Step 5: The acoustic field information saved in steps 3 and 4 can be imaged by Eq. (6), which is only the imaging result of one excitation in practice. The final FRTM image can be obtained by performing the above calculations based on FMC data collected from all single shots and cumulatively summed.

III. SIMULATION

A. MODEL

The 2D BOC model in the aluminum is built in MATLAB, as shown in Fig. 3. Four simplified ultrasonic propagation paths are also drawn in the model to illustrate the imaging results. In the model, the size of the BOC is 1 mm × 5 mm, and it is placed in the middle of the bottom. The longitudinal wave velocity in the aluminum is set to 6260 m/s, while the acoustic velocity of the BOC is set to 340 m/s. There is a linear ultrasonic array with 64 elements used for transmission and reception, and the element pitch is 1mm. The input signal

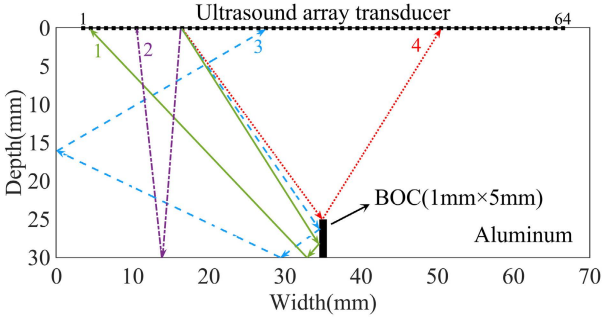

FIGURE 3. The BOC model and the four simplified ultrasonic propagation paths.

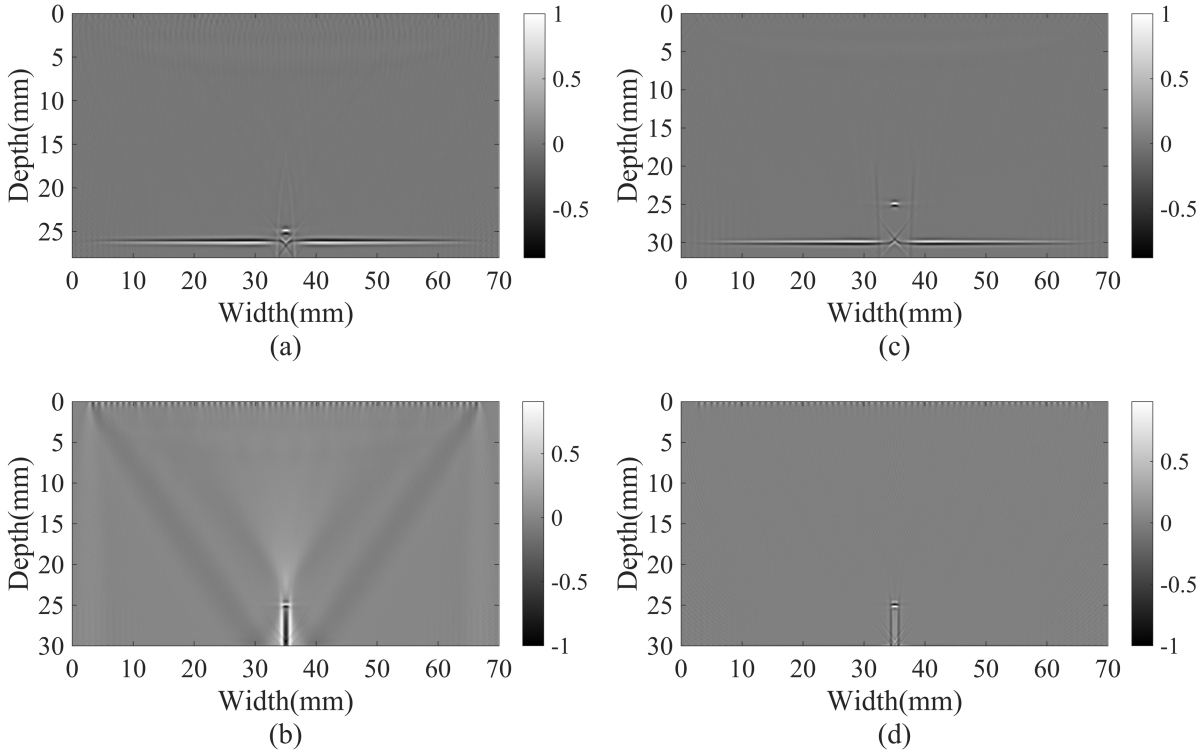

FIGURE 4. Imaging results with different bottom depths set in the FRTM algorithm. (a) The bottom surface depth is set at 28 mm and without the Laplacian filter; (b) The bottom surface depth is set at 30 mm and without the Laplacian filter; (c) The bottom surface depth is set at 32 mm and without the Laplacian filter; (d) The bottom surface depth is set at 30 mm and with the Laplacian filter.

is a half-wavelength delayed Rake wavelet with a center frequency of 5 MHz. The echo signals are recorded for 15 μs with a sampling frequency of 50 MHz.

B. RESULT

In the FRTM algorithm, the excitation source selects the Rake wavelets delayed by half a wavelength, 9 grids are placed at each wavelength, and the whole frequency band is used for imaging. According to the imaging steps in Section 2.5, after inputting the collected data into the FRTM algorithm with the bottom reflective surface set to 28 mm, 30 mm, and 32 mm. Thus, the results without Laplace filtering are shown in Fig. 4(a), Fig. 4(b), and Fig. 4(c), respectively. The reason for obtaining different imaging results can be found in Fig. 3. Using the bottom surface where the ultrasonic wave is reflected, the ultrasonic wave carrying the information of the defect position is reversed to the defect position for imaging, such as the opposite direction of the path 1, and the path 3 is not considered because the PML is set on the side. Therefore, the incorrect bottom surface causes the ultrasonic wave to reverse the path incorrectly, which causes the defect not to be imaged correctly.

In Fig. 4(a), the bottom depth in the algorithm is smaller than the actual bottom depth, which leads to the upward shift of the bottom surface in the imaging results. It is easy to find that the upward moving distance of the interface is 2 mm, and the sum of 2 mm and the bottom surface depth set in the algorithm is 30 mm. This is caused by the reduction in the propagation distance of the ultrasonic waves to the bottom surface. The information on the top of the defect is accurate because the top interface of the defect is still above the bottom surface set in the algorithm and path 4 in Fig. 3 can be fully utilized to image the top of the defect. Similarly, when the depth of the bottom surface in the algorithm is less than the depth of the upper surface of the defect, the upper surface of the defect in the imaging result will also be inaccurate.

In Fig. 4(c), the bottom surface depth in the algorithm is larger than the actual bottom surface depth. Therefore, a single reflected ultrasonic wave can be used to identify the upper interface, such as paths 3 and 4 in Fig. 3. Since the bottom surface in the imaging result, in this case, is accurate, it can be used for bottom identification. If the PML is added to the bottom, the effect of bottom identification will be better because only ultrasonic waves like paths 2 and 4 in Fig. 3 are used and the interference of other ultrasonic waves is excluded.

As mentioned before, accurate and complete imaging of the BOC can only be performed with the correct bottom set in the FRTM, as shown in Fig. 4(b). When the bottom is specified at 30 mm and a Laplace filter is applied, the imaging result is shown in Fig. 4(d). Comparing Fig. 4(b) and Fig. 4(d), the Laplace filter can remove artifacts in the image. The artifact is caused by the mismatch between the forward and the reverse acoustic field [30], [31].

In this subsection, the theory of the FRTM is validated, and the importance of the setting of the bottom surface in the FRTM is illustrated. Further discussion will be realized in the experimental section.

IV. EXPERIMENT

A. EXPERIMENTAL SETUP

Fig. 5 shows the experimental system setup. A multiplexer (MUX-128D-E, Japan Probe) with 128 independent channels is connected to the ultrasonic pulser-receiver (JPR-600C, Japan Probe), and the ultrasonic signals are displayed on the PC terminal. A commercial ultrasound array (Guangzhou Doppler Electronics Technology Co., Ltd.) is used for data acquisition, and the detailed parameters of the array are illustrated in Tab. 1. Fig. 6 shows the physical image of the aluminum block and the ultrasonic array transducer, where the longitudinal wave velocity in the aluminum block is 6260 m/s. In the experiment, the voltage is set to 40 V, the wave number and the gain are set to 1 and 0, respectively, the FFT filter is selected from the range of 3 MHz − 7 MHz, and the echo signals are recorded for 15 μs with a sampling frequency of 50 MHz.

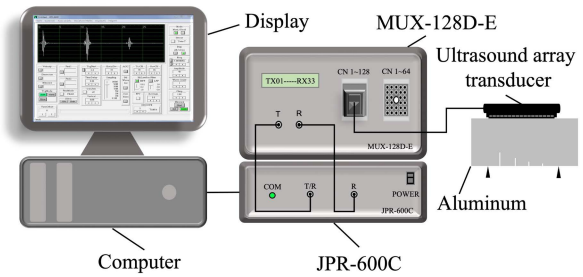

FIGURE 5. The experimental system.

TABLE 1. Ultrasound array transducer parameters.

Parameters	value
Number of elements	128
Element pitch	1 mm
Element size (width, height)	(0.9 mm, 10 mm)
Center frequency	5 MHz
Bandwidth	120%

B. BOTTOM IDENTIFICATION

In the FRTM algorithm, the excitation sequence is generated using the Rake wavelets delayed by half a wavelength, and 9 grids are placed at each wavelength. For imaging processing, the full frequency band is used imaging, the model's width is set to 135 mm, and the depth of the bottom surface is set to 40 mm. In addition, the upper, lower, left, and right borders of the model are all set with 20 layers of PML. The imaging results without the Laplacian filter are shown in Fig. 7. In Fig. 7, it can be seen that only the lower bottom

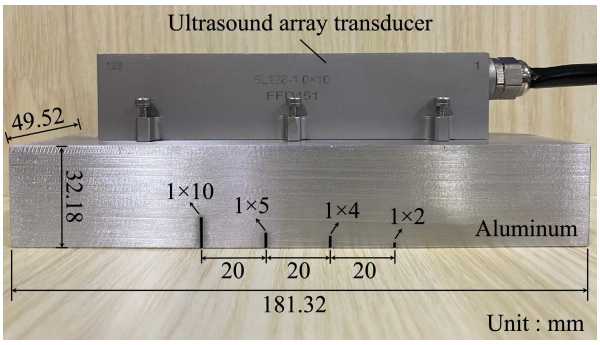

FIGURE 6. The physical image of the aluminum block and the ultrasonic array transducer.

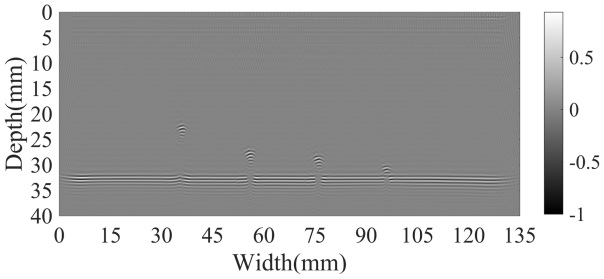

FIGURE 7. The FRTM results with an imaging depth of 40mm and the PML added to the bottom.

surface of the aluminum block and the upper surface of the defect can be confirmed, and the reason for this situation is similar to that of Fig. 4(c).

Next, the values of all the pixel points at the width of 45 mm in Fig. 7 are extracted, and the trace is shown in Fig. 8(a) can be obtained. It can be found that a maximum of the trace occurs between the depth of 30 mm to 35 mm, which corresponds to the position of the bottom surface in Fig. 7. In this way, the position of the largest pixel points of all width coordinates can be extracted, and the extracted data position is shown in Fig. 8(b). The median 32.97 mm of the extracted points is also marked in Fig. 8(b). The data points at the bottom of the aluminum block are the majority, and the data points at the non-bottom are very few, so the median extracted is always the data points at the bottom of the aluminum block.

Therefore, through quantitative evaluation, the depth of the bottom surface can be obtained as 32.97 mm. Since there is a coupling layer between the workpiece and the transducer during the actual inspection, the obtained depth value deviates from the true value, and this error is 2.45%. The obtained depth value is then input to the FRTM program, and the imaging result is shown in Fig. 9.

Artifacts appear around the BOC in Fig. 9(a), which become less pronounced in Fig. 9(b) due to the use of the Laplacian filter. Furthermore, the conventional TFM is used to image the BOC [32], with the same data as used in Fig. 9, and the imaging result is shown in Fig. 10.

Comparing Fig. 10 and Fig. 9, it is easy to confirm the superiority of the FRTM. The TFM can only image the upper surface of the BOC, while the FRTM can image the entire

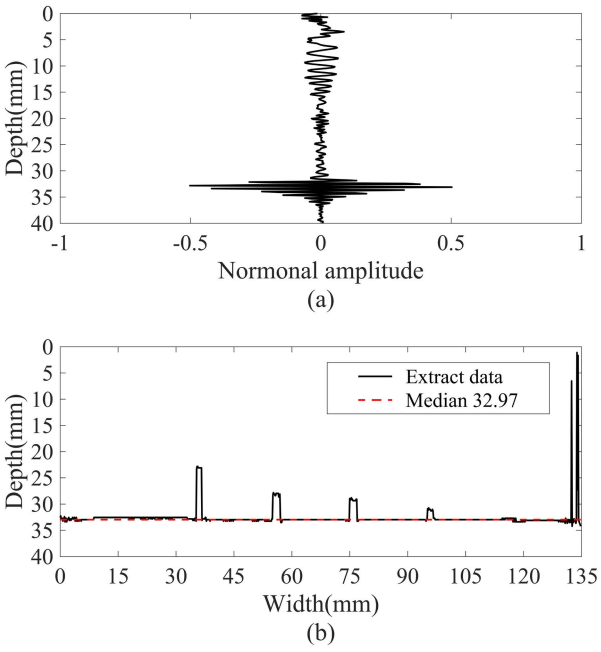

FIGURE 8. The bottom identification. (a) The trace at 45mm of abscissa; (b) Interface extraction.

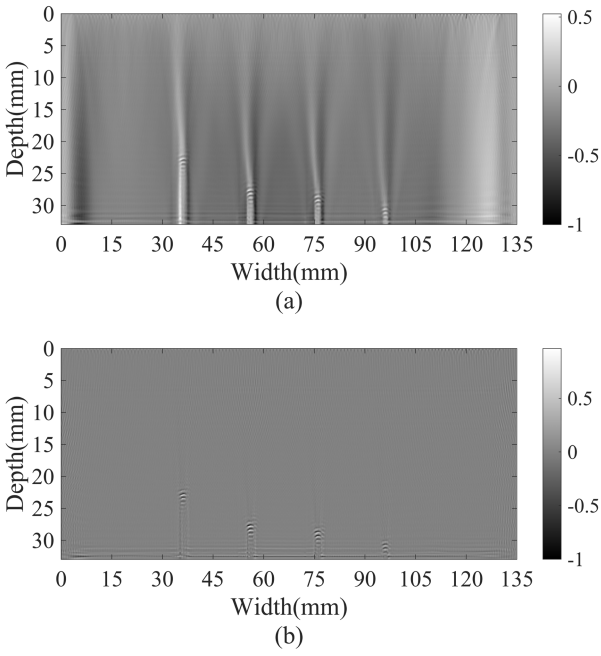

FIGURE 9. The FRTM results of the BOC. (a) The Laplacian filter is not used; (b) The Laplacian filter is used.

outline of the BOC. After the BOC is completely imaged, combined with the results in Fig. 8(b), intuitive quantitative analysis of the BOC can be performed. Since the width of the BOC is consistent, only the quantitative analysis of the height of the BOC is given here. In Fig. 8(b), the length of the BOC can be obtained by subtracting the median of the aluminum block position from the median of the BOC top position. Because the bottom position of the BOC is

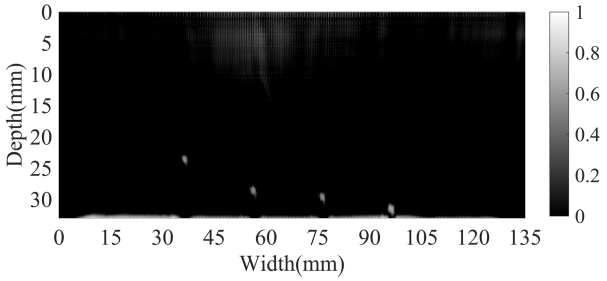

FIGURE 10. The TFM results of the BOC.

TABLE 2. The quantitative analysis of the BOC length.

Actual length(mm)	Measurements(mm)	Error
10	9.8769	-1.23%
5	4.8689	-2.62%
4	3.7560	-6.10%

consistent with the bottom position of the aluminum block, to keep the same way of obtaining the position, the median is used for quantitative analysis. The quantitative analysis results of the BOCs are shown in Tab. 2. Due to the existence of systematic and accidental errors, the quantitative analysis results may deviate from the actual values. The systematic errors are usually related to the stability and sensitivity of the instruments and transducers, and the accidental errors mainly come from the coupling layer. But as can be seen from Tab. 2, the error of this quantitative analysis is very small, and it can be used to perform a very intuitive quantitative analysis of defects.

C. OPTIMIZATION OF THE FREQUENCY CALCULATION RANGE

Fig. 11(a) shows the ultrasonic wave received by the 60th element when the 64th element transmits. After the direct wave is zeroed, the result of FFT using MATLAB is shown in Fig. 11(b), and the whole frequency range is $0-25$ MHz. From Eq. 1, Eq. 2, and Eq. 7, it can be seen that the participation of all frequency components in the imaging calculation will result in a large amount of calculation. Considering the imaging quality and calculating time, the frequency range involved in the imaging calculation can be reduced as much as possible.

As mentioned above, the optimized frequency range is assumed to be [HPF(high pass filter), LPF(low pass filter)]. The value of LPF is determined first, and then it is necessary to set HPF $=$ 0. And the value of LPF can be set to 5 MHz $-$ 25 MHz in the step of 1 MHz. The values of each LPF are individually entered into the FRTM program, and the IQE and computational cost of each imaging are all recorded. Fig. 12 shows the IQE result and computational cost when 9 grids are placed at each wavelength without the Laplace filter in the FRTM algorithm.

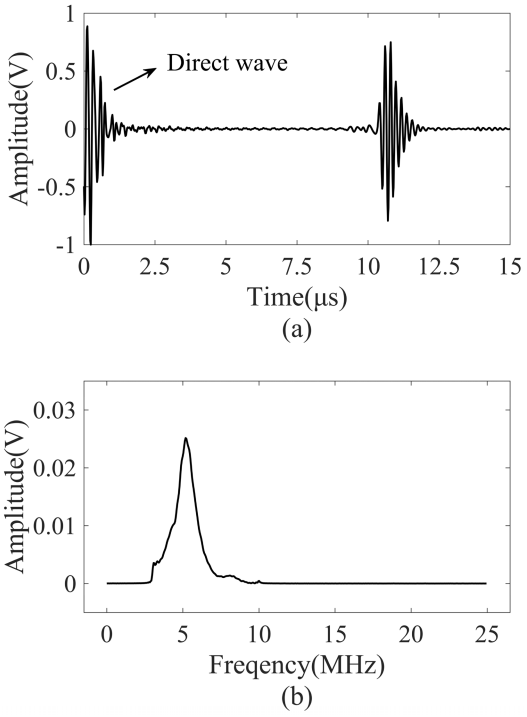

FIGURE 11. The TFM results of the BOC. The primitive wave and the spectrum analysis after removing the direct wave. (a) The primitive wave; (b) The spectrum analysis after removing the direct wave.

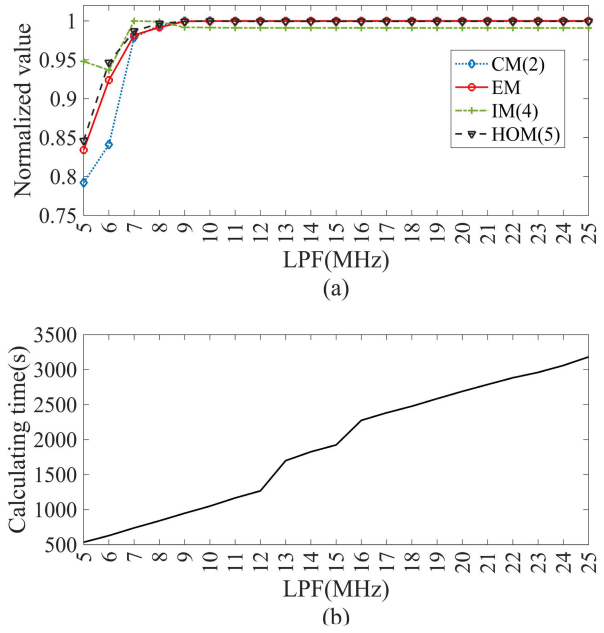

FIGURE 12. Determine the LPF. (a) The IQE of the different LPF values; (b) The calculating time of the different LPF values.

Fig. 12(a) shows the normalization IQE result values. It should be noted that the closer the IQE value is to 1, the better the imaging quality is. The IQE values of the four methods tend to be stable when LPF = 9 MHz. Meanwhile, the IQE values are not low when LPF = 7 MHz. It can be seen from Fig. 12(b) that the imaging calculation time of the FRTM increases with the increase of the calculation frequency band. If all frequencies are involved in the calculation, the maximum calculating time can reach 3181.23 s. Therefore, it is very necessary to determine the calculation range of the frequency band. Based on the current results, the LPF can be set to 9 MHz or 7 MHz.

In the next evaluation, LPF is set to 7 MHz and 9 MHz separately to determine the value of the HPF. First, the value of HPF is set to $0 - 5$ MHz in the step of 1 MHz. Similar results to Fig. 12 can be obtained, as shown in Fig. 13.

Next, comparing the characteristics of Fig. 13(a) and Fig. 13(c), under the condition of ensuring high image quality, the optimal HPF value can be found. Whether LPF = 9 MHz or LPF = 7 MHz, the HPF value of 4 MHz is a better option. Although in the IM(4) method, the maximum value at HPF = 5 MHz, it is obviously unreasonable to set 5 MHz because the center frequency of the used ultrasound array is 5 MHz. In Fig. 13(b) and Fig. 13(d), when LPF = 7 MHz, the imaging computation cost is shorter. In contrast, when HPF = 4 MHz, the accurate imaging time of the LPF of 9 MHz and 7 MHz are 526.111 s and 314.828 s, respectively. Also, the imaging results of these two cases are shown in Fig. 14.

The results shown in Fig. 14 confirm that the imaging with LPF of 9 MHz and 7 MHz are not significantly different. After using the Laplace filter, the side profile of the BOCs can all be clearer, and the artifacts in the BOCs can be removed. Interestingly, the imaging computation time is shorter when LPF = 7 MHz. In conclusion, the optimized frequency calculation range is set to [4 MHz, 7 MHz].

D. OPTIMIZATION OF THE NUMBER OF GRID POINTS PLACED AT EACH WAVELENGTH

The number of grid points placed at each wavelength is defined as Num, and it can be observed from Eq. 2 and Eq. 7 that a larger Num means a larger amount of calculation. Therefore, it is also necessary to find a suitable Num. With the frequency range set to [4 MHz, 7 MHz], the minimum Num preliminarily explored. After testing, when the BOC can be observed, the minimum value of Num is 4, and the calculating time is only 66.2048 s. The specific imaging result is shown in Fig. 15.

Further, considering the IQE value and calculating time, Num is reduced as much as possible, and the range of Num is set to $4 - 15$ in 1 step. Similar results to Fig. 12 can be obtained, as shown in Fig. 16.

In Fig. 16(a), except for Num = 4, the IQEs of four methods all show the first maximum point at Num = 6. The overall trend of CM(2), EM, and IM(4) are basically unchanged as Num increases. HOM(5) has maximum points at Num = 6, 9, and 12. In Fig. 16(b), the larger the Num, the larger the imaging computation time. Therefore, considering the IQE and the imaging calculation time, Num = 6 is the best option. The imaging result, in this case, is shown in Fig. 17, and the imaging calculation time is 175.922 s.

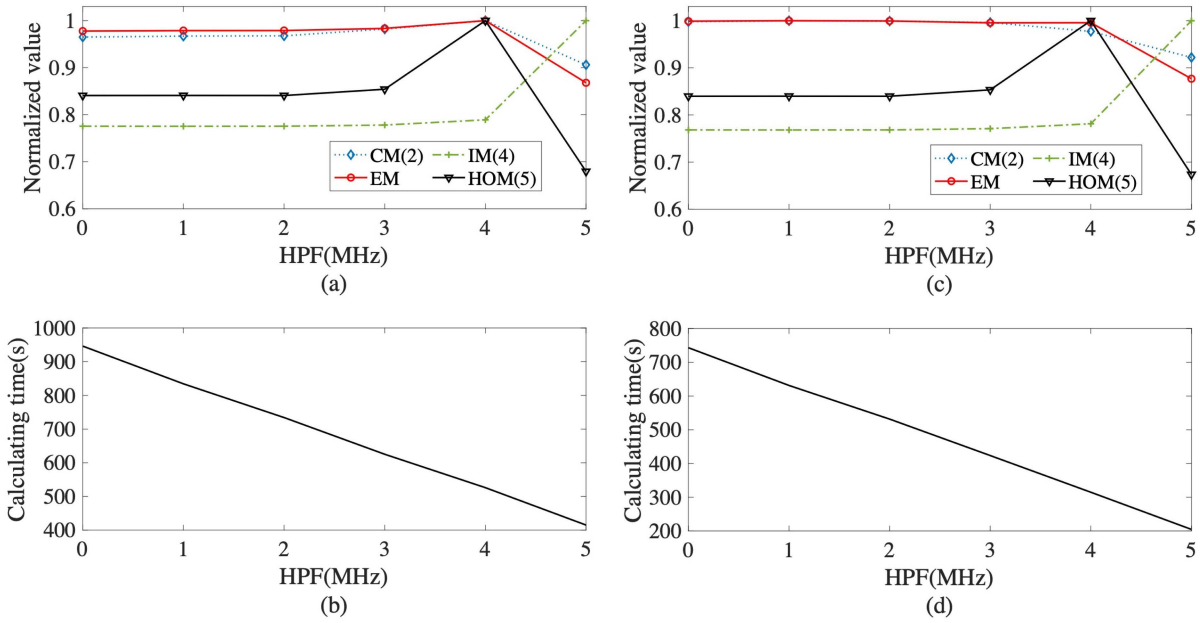

FIGURE 13. Determine the HPF. (a) When LPF = 9 MHz, the IQE of the different HPF values; (b) When LPF = 9 MHz, the calculating time of the different LPF values; (c) When LPF = 7 MHz, the IQE of the different HPF values; (d) When LPF = 7 MHz, the calculating time of the different LPF values.

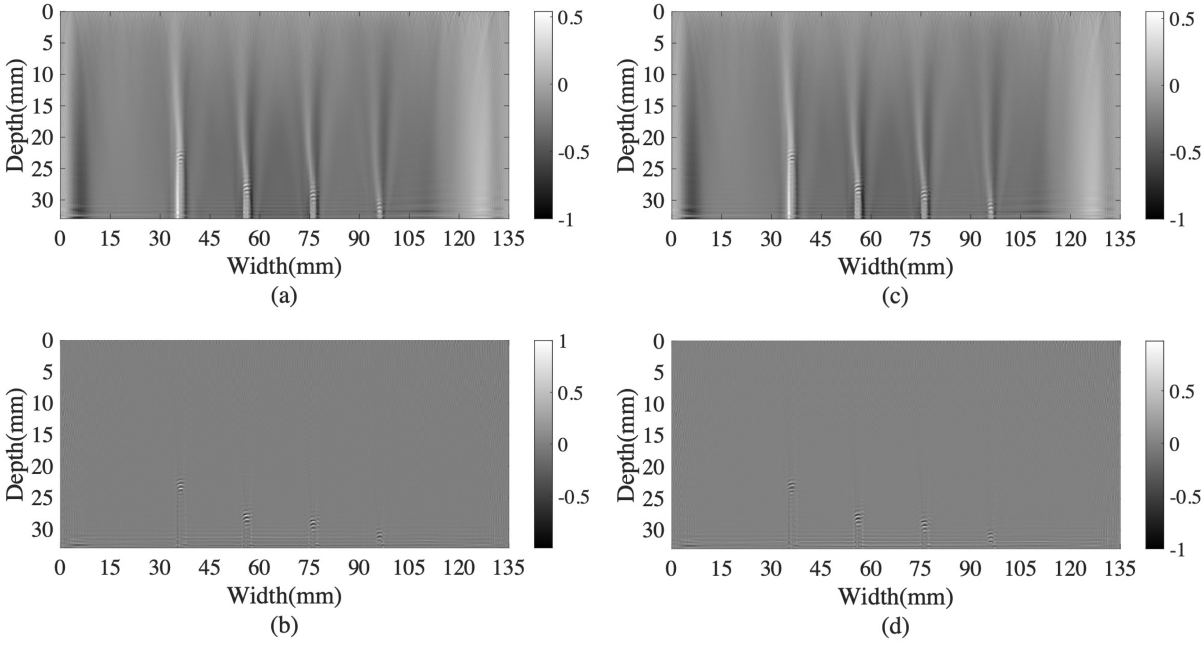

FIGURE 14. The imaging results when HPF = 4 MHz and LPF is 9 MHz or 7 MHz, respectively. (a) When LPF = 9 MHz and without the Laplacian filter; (b) When LPF = 9 MHz and using the Laplacian filter; (c) When LPF = 7 MHz and without the Laplacian filter; (d) When LPF = 7 MHz and using the Laplacian filter.

As shown in Fig. 17, the optimized imaging results are highly consistent with that of Fig. 9 without optimization. At the same time, the imaging calculation time is reduced from 3181.23 s to 175.922 s, which is about 1/18 of the original time. When Num = 4, the imaging calculation time is only 66.2048*s*, and the calculation speed is naturally greatly accelerated.

V. DISCUSSIONS

In subsection 4.2, this research proposed to use FRTM, although other imaging algorithms such as the B-scan can also be used for interface identification [18]. This is because FRTM is obviously more versatile, and it is beneficial to eliminate the errors that different imaging algorithms may cause. The imaging calculation is performed on a single

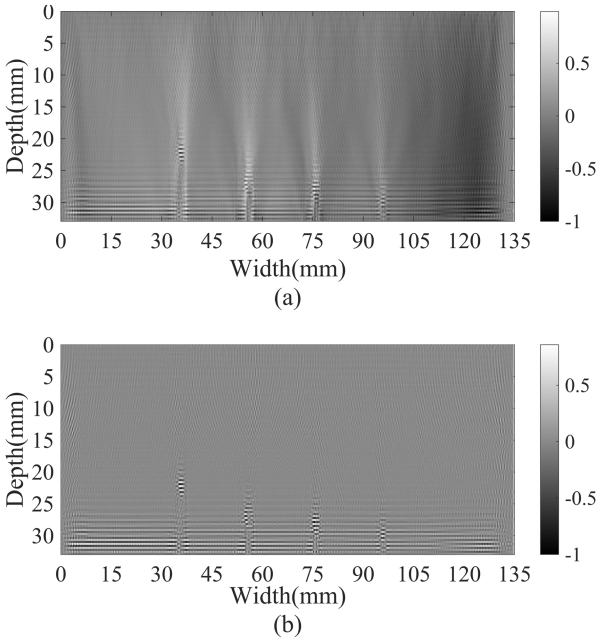

FIGURE 15. The imaging results with 4 grid points placed at each wavelength. (a) The Laplacian filter is not used; (b) The Laplacian filter is used.

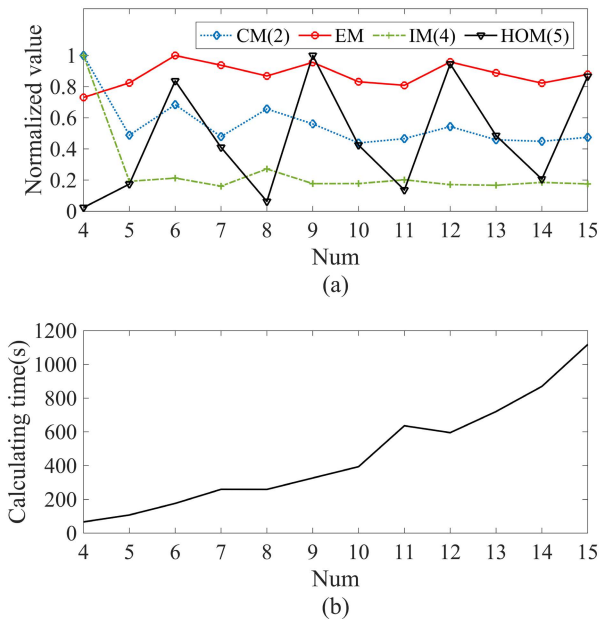

FIGURE 16. Determine the Num. (a) The IQE of the different Num; (b) The calculating time of the different Num.

computer. The CPU model is 10-Core Intel Core i9, the operating system is macOS Catalina, and the MATLAB version is 2021a. By default, the built-in parfor in MATLAB is used for parallel calculation. This algorithm has high requirements on the running speed of the computer. But since the optimization direction of this study is to reduce the amount of computation in the algorithm, which is a more general

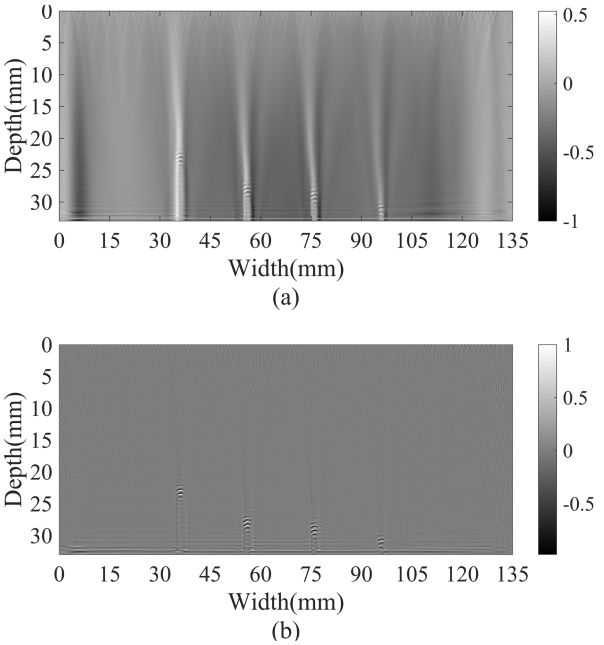

FIGURE 17. The imaging results when Num = 6. (a) The Laplacian filter is not used; (b) The Laplacian filter is used.

process for imaging. The program can run more efficiently if processes such as GPU acceleration and cluster acceleration of multiple computers [33], [34].

VI. CONCLUSION

In this study, the FRTM method based on the optimal 9-point FDM is successfully proposed in the field of ultrasonic NDT. This method can fully image the BOC, which is difficult to achieve by traditional ultrasonic imaging methods. The application of the method to bottom identification also facilitates the complete imaging and quantitative analysis of the defect. In addition, the specific optimization method of the algorithm is also given. The frequency range used for imaging calculations and the number of grid points placed at each wavelength were optimized, considering the imaging quality and computational cost. It is undeniable that these optimization items significantly shorten the imaging cycle.

In the next stage, this method will be used to study real-time imaging of complex multilayer media.

REFERENCES

[1] R. Wang, Q. Wu, F. Yu, Y. Okabe, and K. Xiong, "Nonlinear ultrasonic detection for evaluating fatigue crack in metal plate," *Structural Health Monitor.*, vol. 18, no. 3, pp. 869–881, May 2019.

[2] H. Lim and H. Sohn, "Fatigue crack detection using structural nonlinearity reflected on linear ultrasonic features," *J. Appl. Phys.*, vol. 118, no. 24, p. 7453, 2015.

[3] B. W. Drinkwater and P. D. Wilcox, "Ultrasonic arrays for non-destructive evaluation: A review," *NDT E Int.*, vol. 39, no. 7, pp. 525–541, Oct. 2006.

[4] N. Portzgen, D. Gisolf, and G. Blacquiere, "Inverse wave field extrapolation: A different NDI approach to imaging defects," *IEEE Trans. Ultrason., Ferroelectr., Freq. Control*, vol. 54, no. 1, pp. 118–127, Jan. 2007.

[5] Z. Bai, S. Chen, L. Jia, and Z. Zeng, "Phased array ultrasonic signal compressive detection in low-pressure turbine disc," *NDT E Int.*, vol. 89, pp. 1–13, Jul. 2017.

[6] Z. Han, H. Peng, and P. Lu, "3D ultrasound imaging in frequency domain with 1D array transducer," *Ultrasonics*, vol. 76, pp. 28–34, Apr. 2017.
[7] A. Saini, M. V. Felice, Z. Fan, and C. J. L. Lane, "Optimisation of the half-skip total focusing method (HSTFM) parameters for sizing surface-breaking cracks," *NDT E Int.*, vol. 116, Dec. 2020, Art. no. 102365.
[8] C. J. Leuschen and R. G. Plumb, "A matched-filter-based reverse-time migration algorithm for ground-penetrating radar data," *IEEE Trans. Geosci. Remote Sens.*, vol. 39, no. 5, pp. 929–936, May 2001.
[9] J. M. Zhu and L. R. Lines, "Comparison of Kirchhoff and reverse-time migration methods with applications to prestack depth imaging of complex structures," *Geophysics*, vol. 63, no. 4, pp. 1166–1176, May 1998.
[10] D. D. Kosloff and E. Baysal, "Forward modeling by a Fourier method," *Geophysics*, vol. 47, no. 10, pp. 1402–1412, 1982.
[11] M. Dablain, "The application of high-order differencing to the scalar wave equation," *Geophysics*, vol. 51, no. 1, pp. 54–66, Jan. 1986.
[12] S. Müller, E. Niederleithinger, and T. Bohlen, "Reverse time migration: A seismic imaging technique applied to synthetic ultrasonic data," *Int. J. Geophys.*, vol. 2012, pp. 1–7, Apr. 2012.
[13] S. Beniwal and A. Ganguli, "Reverse time migration based ultrasonic imaging of rebars embedded in concrete," in *Proc. IEEE Int. Ultrason. Symp. (IUS)*, Oct. 2015, pp. 1–4.
[14] Y. Qi, Z. Chen, H. Liu, Y. Qi, H. Tong, and J. Xie, "Ultrasonic inspection of prefabricated constructions using reverse time migration imaging method," in *Proc. IEEE Int. Conf. Signal, Inf. Data Process. (ICSIDP)*, Dec. 2019, pp. 1–4.
[15] J. Rao, A. Saini, J. Yang, M. Ratassepp, and Z. Fan, "Ultrasonic imaging of irregularly shaped notches based on elastic reverse time migration," *NDT E Int.*, vol. 107, Oct. 2019, Art. no. 102135.
[16] E. Lubeigt, S. Mensah, S. Rakotonarivo, J.-F. Chaix, F. Baqué, and G. Gobillot, "Topological imaging in bounded elastic media," *Ultrasonics*, vol. 76, pp. 145–153, Apr. 2017.
[17] J. Chang, C. Wang, Y. Tang, and W. Li, "Numerical investigations of ultrasonic reverse time migration for complex cracks near the surface," *IEEE Access*, vol. 10, pp. 5559–5567, 2022.
[18] X. Yang, K. Wang, Y. Xu, L. Xu, W. Hu, H. Wang, and Z. Su, "A reverse time migration-based multistep angular spectrum approach for ultrasonic imaging of specimens with irregular surfaces," *Ultrasonics*, vol. 108, Dec. 2020, Art. no. 106233.
[19] H. Liu, Z. Long, F. Han, G. Fang, and Q. H. Liu, "Frequency-domain reverse-time migration of ground penetrating radar based on layered medium Green's functions," *IEEE J. Sel. Topics Appl. Earth Observ. Remote Sens.*, vol. 11, no. 8, pp. 2957–2965, Aug. 2018.
[20] S. A. Levin, "Principle of reverse-time migration," *Geophysics*, vol. 49, no. 5, pp. 581–583, 1984.
[21] C.-H. Jo, C. Shin, and J. H. Suh, "An optimal 9-point, finite-difference, frequency-space, 2-D scalar wave extrapolator," *Geophysics*, vol. 61, no. 2, pp. 529–537, 1996.
[22] B. Hustedt, S. Operto, and J. Virieux, "Mixed-grid and staggered-grid finite-difference methods for frequency-domain acoustic wave modelling," *Geophys. J. Int.*, vol. 157, no. 3, pp. 1269–1296, 2004.
[23] C. Shin, D. J. Min, D. Yang, and S. K. Lee, "Evaluation of poststack migration in terms of virtual source and partial derivative wavefields," *J. Seismic Explor.*, vol. 12, no. 1, pp. 17–37, 2003.
[24] W. Chung, S. Pyun, H. S. Bae, C. Shin, and K. J. Marfurt, "Implementation of elastic reverse-time migration using wavefield separation in the frequency domain," *Geophys. J. Int.*, vol. 189, no. 3, pp. 1611–1625, Jun. 2012.
[25] A. Guitton, B. Kaelin, and B. Biondi, "Least-squares attenuation of reverse-time-migration artifacts," *Geophysics*, vol. 72, no. 1, pp. S19–S23, Jan. 2007.
[26] O. K. Youn and H. Zhou, "Depth imaging with multiples," *Geophysics*, vol. 66, no. 1, pp. 246–255, Jan. 2001.
[27] X. Wei and Y. Zhang, "Autofocusing techniques for GPR data from RC bridge decks," *IEEE J. Sel. Topics Appl. Earth Observ. Remote Sens.*, vol. 7, no. 12, pp. 4860–4868, Dec. 2014.
[28] H. Jung and K. Kim, "Autofocusing technique based on generalized multilayer Stolt migration," *IEEE Trans. Geosci. Remote Sens.*, vol. 56, no. 3, pp. 1386–1393, Mar. 2018.
[29] B. Finkelstein and R. Kastner, "Finite difference time domain dispersion reduction schemes," *J. Comput. Phys.*, vol. 221, no. 1, pp. 422–438, Jan. 2007.
[30] F. Moradpouri, A. Moradzadeh, R. Pestana, R. Ghaedrahmati, and M. S. Monfared, "An improvement in wavefield extrapolation and imaging condition to suppress reverse time migration artifacts," *Geophysics*, vol. 82, no. 6, pp. S403–S409, Nov. 2017.
[31] F. Moradpouri, A. Moradzadeh, R. C. Pestana, and M. S. Monfared, "Seismic reverse time migration using a new wave-field extrapolator and a new imaging condition," *Acta Geophys.*, vol. 64, no. 5, pp. 1673–1690, Oct. 2016.
[32] C. Holmes, B. W. Drinkwater, and P. D. Wilcox, "Advanced post-processing for scanned ultrasonic arrays: Application to defect detection and classification in non-destructive evaluation," *Ultrasonics*, vol. 48, nos. 6–7, pp. 636–642, 2008.
[33] H.-W. Liu, B. Li, H. Liu, X.-L. Tong, and Q. Liu, "The algorithm of high order finite difference pre-stack reverse time migration and GPU implementation," *Chin. J. Geophys.*, vol. 53, no. 4, pp. 600–610, Jul. 2010.
[34] S. Y. Suh, A. Yeh, B. Wang, J. Cai, K. Yoon, and Z. Li, "Cluster programming for reverse time migration," *Lead. Edge*, vol. 29, no. 1, pp. 94–97, Jan. 2010.